

A complex storm system in Saturn's north polar atmosphere in 2018

A. Sánchez-Lavega^{1*}, E. García-Melendo^{2*}, J. Legarreta³, R. Hueso¹, T. del Río-Gaztelurrutia¹, J. F. Sanz-Requena^{4,5}, S. Pérez-Hoyos¹, A. A. Simon⁶, M. H. Wong⁷, M. Soria⁸, J. M. Gómez-Forrellad⁹, T. Barry¹⁰, M. Delcroix¹¹, K. M. Sayanagi¹², J. J. Blalock¹², J. L. Gunnarson¹², U. Dyudina¹³ and S. Ewald¹³

Saturn's convective storms usually fall in two categories. One consists of mid-sized storms ~2,000 km wide, appearing as irregular bright cloud systems that evolve rapidly, on scales of a few days. The other includes the Great White Spots, planetary-scale giant storms ten times larger than the mid-sized ones, which disturb a full latitude band, enduring several months, and have been observed only seven times since 1876. Here we report a new intermediate type, observed in 2018 in the north polar region. Four large storms with east-west lengths ~4,000–8,000 km (the first one lasting longer than 200 days) formed sequentially in close latitudes, experiencing mutual encounters and leading to zonal disturbances affecting a full latitude band ~8,000 km wide, during at least eight months. Dynamical simulations indicate that each storm required energies around ten times larger than mid-sized storms but ~100 times smaller than those necessary for a Great White Spot. This event occurred at about the same latitude and season as the Great White Spot in 1960, in close correspondence with the cycle of approximately 60 years hypothesized for equatorial Great White Spots.

Saturn's convective storms of both mid- and planetary scale have been imaged at optical and near-infrared wavelengths from the Voyager 1 and Voyager 2 spacecrafts^{1–3}, the Hubble Space Telescope (HST)^{4–6}, ground-based telescopes and the Cassini spacecraft^{7–9}. Cassini also detected radio emissions and bright flashes associated with lightning in the storms^{10–12}. These storms result from moist convection in the upper cloud layers^{13,14} and play a substantial role in Saturn's atmospheric dynamics^{8,9,15,16}.

We observed Saturn from Earth during its entire 2018 apparition. This report is primarily based on the analysis of >500 telescopic images obtained in the visual range, provided by a network of 81 observers contributing to the Planetary Virtual Observatory and Laboratory (PVOL)¹⁷ and the Association of Lunar and Planetary Observers in Japan (ALPO-Japan) open repositories (Supplementary Table 1). Additional images in the visual and near-infrared spectral ranges were obtained during three observing runs (May, June and September 2018) with the 2.2-m telescope at Calar Alto Observatory using the camera PlanetCam¹⁸. We have also used images obtained on 6–7 June 2018 with the Wide Field Planetary Camera (WFPC) of the HST, pertaining to the Outer Planet Atmospheres Legacy (OPAL) programme¹⁹. Finally, images captured between December 2016 and September 2017 by the Imaging Science Subsystem (ISS) camera onboard NASA's Cassini spacecraft were used to identify a precursor of the first storm as described in the following section. Details on the observations and image analysis are given in the Methods and Supplementary Information. Our study concentrates on the period from 29 March

(date of discovery of the first storm) to 21 November. In this period, unusual bright spots emerged between latitudes 67°N and 74°N, on the north side of a double-peaked eastward jet^{3,20}, reaching Saturn's hexagon border.

Evolution of convective storms

The first storm, White Spot 1 (WS1), was imaged on 29 March (day $t=0$ d) as a bright spot of dimensions 10° east–west and 4° north–south (~4,000 km), at latitude 67.4°N within a region of cyclonic vorticity (Figs. 1 and 2, Supplementary Fig. 1). Latitudes are planetographic (φ) throughout unless otherwise noted. By 1 April ($t=3$ d) the clouds had expanded westward and eastward at the north and south edges respectively, in agreement with the direction of the meridional shear of the zonal winds at this latitude^{3,20}. WS1 remained a compact spot; to the east and west of WS1, other spots of smaller size and brightness formed. On 25 May ($t=56$ d) a second bright spot (WS2) was observed, 30° to the west and 0.7° north of WS1 (Fig. 1b). Higher resolution HST images from 6 June show that both WS1 and WS2 consist of 3–4 smaller spots from which zonally elongated filaments extend, oriented according to the meridional wind shear (Fig. 1c, Supplementary Fig. 1). By 17–18 June ($t=81$ d), WS2 developed a tail, grew in longitude and a third distinct bright spot (WS3) formed to the northwest of WS2, separated by 20° in longitude and at 72°N in latitude (Fig. 1d–f). A fourth, short-lived spot (WS4) formed on 13 August ($t=137$ d) at latitude 74.3°N, 0.7° south of the hexagon border (Fig. 1k). We tracked WS1 and WS2 until late October 2018, when the spots ceased to be detected,

¹Departamento Física Aplicada I, Escuela de Ingeniería de Bilbao, Universidad del País Vasco UPV/EHU, Bilbao, Spain. ²Serra Hünter Fellow, Escola Superior d'Enginyeries Industrial, Aeroespacial i Audiovisual, UPC, Terrasa, Spain. ³Departamento de Ingeniería de Sistemas y Automática, Escuela de Ingeniería de Bilbao, Universidad del País Vasco UPV/EHU, Bilbao, Spain. ⁴Departamento de Ciencias Experimentales, Universidad Europea Miguel de Cervantes, Valladolid, Spain. ⁵Departamento de Física Teórica, Atómica y Óptica; Facultad de Ciencias, Universidad de Valladolid, Valladolid, Spain. ⁶NASA Goddard Space Flight Center, Greenbelt, MD, USA. ⁷University of California Berkeley, Berkeley, CA, USA. ⁸Escola Superior d'Enginyeries Industrial, Aeroespacial i Audiovisual, UPC, Terrasa, Spain. ⁹Fundació Observatori Esteve Duran, Barcelona, Spain. ¹⁰Broken Hill Observatory, Broken Hill, New South Wales, Australia. ¹¹Société Astronomique de France, Paris, France. ¹²Hampton University, Hampton, VA, USA. ¹³California Institute of Technology, Pasadena, CA, USA. *e-mail: agustin.sanchez@ehu.eus; enrique.garcia.melendo@upc.edu

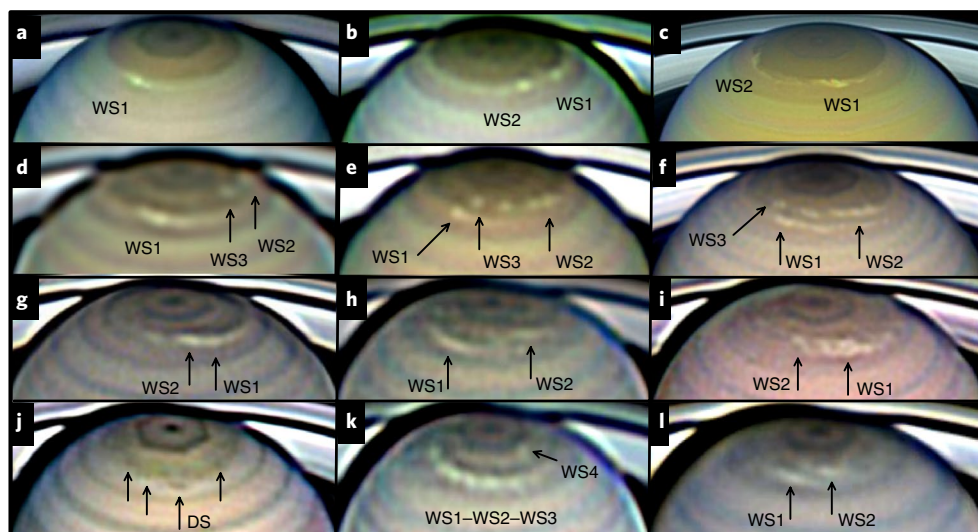


Fig. 1 | The 2018 complex north polar storm system and disturbances. Saturn is shown in a series of images during the 2018 apparition. Each image is cropped such that the bottom edge falls on 47° N latitude at the central meridian. **a**, 1 April (D. Peach). **b**, 26 May (A. Casely). **c**, 6 June (HST-OPAL programme). **d**, 23 June (T. Barry). **e**, 28 June (D. Peach). **f**, 30 June (D. P. Milika and P. Nicholas). **g**, 11 July (B. Macdonald). **h**, 8 August (T. Barry). **i**, 16 August (F. Silva-Correa). **j**, 18 August (D. Peach). **k**, 19 August (T. Barry). **l**, 16 September (B. Macdonald). Names in brackets indicate the observer. DS, dark spot. Identification of features follows the nomenclature given in the text. See also map projections in Supplementary Fig. 1.

resulting in lifetimes of ~ 214 and ~ 157 days respectively. We also measured the longitude drift rate of the storms (ω , $^\circ \text{day}^{-1}$) and other features relative to the System III rotation frame²¹, their zonal velocities (u , m s^{-1}), and their mean latitude (φ) over their lifetimes (Fig. 2, Table 1, Supplementary Figs. 2–3). We find that the velocities of WS2, WS3 and WS4 are very close (by 5 m s^{-1}) to the zonal wind speed at their respective latitudes^{3,20}. WS1 moved about 35 m s^{-1} slower than the wind profile²⁰. Part of this difference could be due to the $\pm 0.7^\circ$ uncertainty in the latitude measurements of the storm (Supplementary Fig. 3). However, we found that a cyclone that was visible north of a coupled three-vortex system in 2015 HST images²², and can be traced in Cassini ISS images at least since 2013, exhibited a good match to WS1 in latitude, longitude and drift rate during the period 2016–2017 (Fig. 3). This indicates that the outbreak WS1 most probably began in that cyclone, similar to the genesis of large convective storms within cyclones observed on Jupiter²³. Because the cyclone was located $+0.5^\circ$ to the north of WS1's mean latitude, but moved with the same velocity (Fig. 3, Table 1), the cyclone moved 15 m s^{-1} slower than the zonal winds²⁰. This is probably also the case for WS1 once the latitude uncertainty is taken into account.

The separation in latitude between the storms resulted in zonal velocities ranging from $+60 \text{ m s}^{-1}$ at 67° N to -5 m s^{-1} at 74° N (Fig. 2, Table 1). Because the storms were close in latitude, there were mutual encounters when a faster WS1 overtook WS2 and when WS1 overtook WS3 (Fig. 2). The interaction between the storms during their close passages generated chains of bright spots along a longitude sector $\sim 100^\circ$ in extent ($\sim 45,000 \text{ km}$) at latitudes $+67^\circ$ and $+71^\circ$ (Fig. 1d–l, Supplementary Fig. 1). Typically these chains consisted of about 7–10 spots with a mean separation of $7,500 \pm 900 \text{ km}$, suggesting that a wave disturbance was triggered during the encounters (Fig. 1k). At other longitudes where no bright spot chain formed, there appeared dark spots (such as DS in Fig. 1j) and other less contrasted spots (indicated by arrows in Fig. 1j), and by July ($t \approx 120 \text{ d}$) all longitudes in the cyclonic side of the jet, within a band from latitudes around $+66^\circ$ to $+73^\circ$, were disturbed (Fig. 1k).

Vertical structure of storm clouds

HST images obtained at different wavelengths (Supplementary Fig. 4) were calibrated in absolute reflectivity (I/F , intensity/solar

flux, as it is conventional in planetary atmospheres)²⁴ and we retrieved centre-to-limb dependence of I/F at each available wavelength both for the storms and adjacent undisturbed areas. We used the NEMESIS (Nonlinear optimal Estimator for Multivariate spectral analysis) radiative transfer code²⁵ to model the upper cloud structure and hazes²⁶ (Methods and Supplementary Fig. 5). The wavelength range covered by HST images allows the sounding of the tropospheric haze and the top level of the upper ammonia cloud^{27,28}. When comparing the storm cloud structure to the surrounding clouds, the model fit to the observations is improved if the storm clouds are denser and slightly higher. The storm model requires an increase in the optical depth of the tropospheric cloud from ~ 10 to 32 (that is, an increase in the particle density from ~ 50 to 215 cm^{-3}), together with an increase in the top altitude of the hazes from ~ 600 to 200 mbar (Fig. 4, Supplementary Tables 2,3). Height of the storm cloud-tops is consistent with their non-detection in ground-based images obtained in the 890-nm methane absorption band, because clouds reaching the tropopause at 60–100 mbar would be detected in that band²⁸. The particles in the storm clouds are marginally brighter (that is, with lower imaginary refractive index) and slightly larger (radius of $0.18 \mu\text{m}$ instead of $0.10 \mu\text{m}$) relative to surrounding clouds, but such variations are within the 1σ retrieval error for these parameters. These properties are consistent with those found for storms observed in the ‘storm alley’ in 2004–2009, as studied using Cassini/Visible and Infrared Mapping Spectrometer (VIMS) 1–5- μm spectra²⁹.

Dynamical simulations

In order to quantify the energy involved in the development of these storms, we have studied the dynamical effects on the atmospheric flow of simulated storms using a shallow water (SW) model³⁰ and the explicit planetary isentropic-coordinate (EPIC) general circulation model^{6,31,32}. Both models represent simplified versions of Saturn's troposphere at the latitude where the storms developed. We simulated a latitudinal domain in which we imposed fluid motions that follow the measured wind profile (that is, the zonal mean velocity as a function of latitude; Fig. 2). We introduce a convective storm in this flow as a localized disturbance with the measured size of the observed spots (WS1 and WS2) and with a certain intensity.

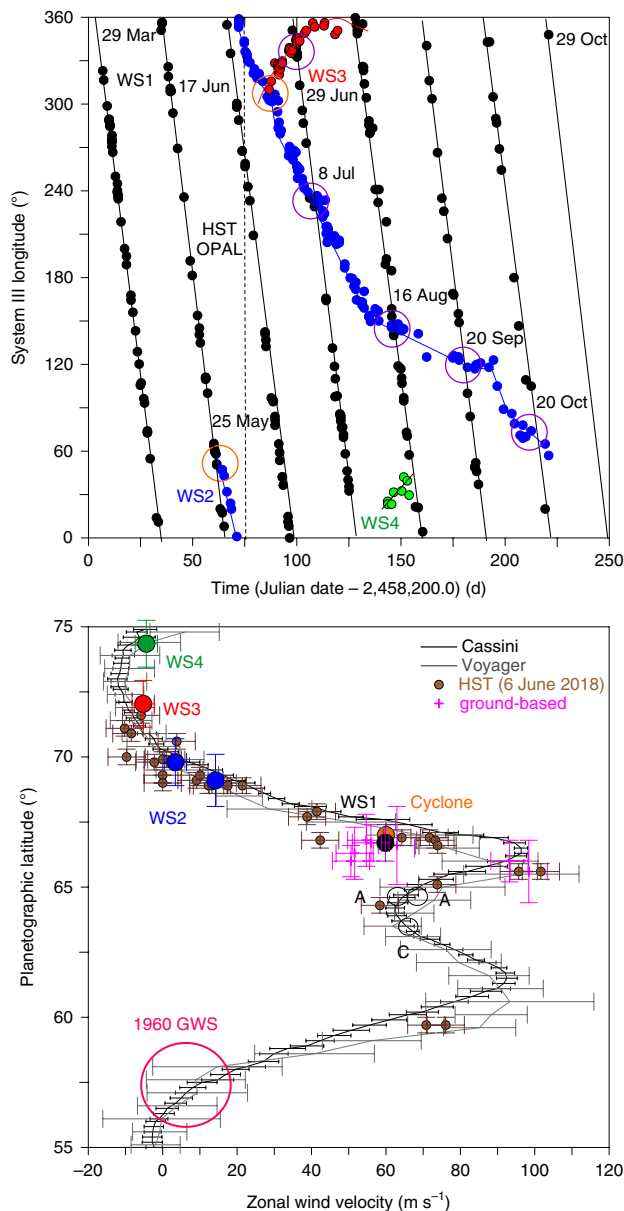


Fig. 2 | Storm motions from 29 March to 29 October 2018. **a**, Black (storm WS1), blue (storm WS2), red (storm WS3) and green (storm WS4) show the motions of the four long-lived storms in System III longitude²¹. Orange circles mark the date and position of the outbreak of WS2 and WS3. Violet circles mark the date of the close encounters between storms: WS1–WS3 (~29 June, $t \approx 93$ d), WS1–WS2 (~8 July, $t \approx 100$ d), WS1–WS2 (~16 August, $t \approx 140$ d), WS1–WS2 (~20 September, $t \approx 174$ d), WS1–WS2 (~20 October, $t \approx 211$ d). The vertical dashed line indicates the HST observation date. **b**, Zonal velocity of the main storms (WS1–WS4) and other features (small brown dots and magenta crosses) pertaining to the disturbance in the averaged wind profile^{3,20}. The orange dot corresponds to the cyclone where WS1 erupted. The long-lived anticyclone–cyclone–anticyclone (ACA) triple vortex is also indicated²². See also Supplementary Figs. 2–3. The location of the 1960 GWS is indicated by a large pink circle^{9,33}. The upper graph has no error bars visible in longitude axis since they are smaller than the dot representing each measurement. The lower graph shows error bars in the wind profile from^{3,20}. The error bars in the individual velocity points from measurements of ground-based and HST images are calculated as follows: in velocity, using the linear fits to the longitude drift rates of the features, and in latitude, from the error in the planet limb navigation and feature pointing. The features latitude error for HST images is $\pm 0.3^\circ$ and in ground-based images ranges from $\pm 0.7^\circ$ to $\pm 1.5^\circ$ (standard deviation from the mean value).

Table 1 | Main polar storm motions

Storm	Onset (2018)	Latitude φ ($^\circ$) ^b	Drift ω ($^\circ$ d ⁻¹)	Zonal velocity u (m s^{-1}) ^c	Tracking time (d)
WS1	25 March	$66.7^\circ \pm 0.7^\circ$ N	-11.5	$+59.8 \pm 1.5$	214
WS2	25 May	$69.1^\circ \pm 1^\circ$ N	-3	$+14.2 \pm 2$	157
WS2 ^a	25 May	$69.8^\circ \pm 0.9^\circ$ N	-0.75	$+3.4 \pm 2$	157
WS3	17 June	$72.04^\circ \pm 0.9^\circ$ N	+1.3	-5.2 ± 2	33
WS4	13 August	$74.3^\circ \pm 0.9^\circ$ N	+1.2	-4.4 ± 2	10

^aWS2 changed in latitude (see Fig. 2 and Supplementary Fig. 2). ^bError in latitude is calculated as the standard deviation of the values used in the linear fit. ^cError in velocity is deduced from the quadratic deviation of the fitted drift.

In the SW model, the storm is initiated by a horizontal Gaussian mass flow with a given amplitude Q ($\text{m}^3 \text{s}^{-1}$). In the EPIC model, the disturbance is introduced as a Gaussian heating source that injects a localized source of energy in the flow E (W kg^{-1}). In both cases, Q , E and the duration of the disturbances, as well as their location in the wind profile (latitude and velocity), determine the evolution of the two-dimensional potential vorticity (PV) field²⁴ that can be compared to the observed cloud morphology^{6,30,31}. In our simulations, the amplitude of the mass injection or heating source are left as free parameters. Other adjustable parameters of the models are described in the Methods and Supplementary Tables 4.1 and 4.2.

In the SW model, we simulated the evolution of storms WS1 and WS2 and their mutual interaction. Our best fit between the observed WS1 and WS2 cloud morphology and the PV field given by the model requires a mass flow injection in the range $Q = 2\text{--}4 \times 10^9 \text{ m}^3 \text{ s}^{-1}$ (Fig. 5). In the model, the encounter between WS1 and WS2 (days 94.5–100 in Fig. 5) generates a zonal disturbance that links both storms resembling the observations (Fig. 1g–i and Supplementary Fig. 1). The disturbed band between WS1 and WS2 contains periodic features with apparent wavelike nature, reminiscent of the observations (Fig. 5, day 100). The interaction between both storms in the model also favours the propagation of the activity poleward of the latitude of WS2 (days 96–120 in Fig. 5) as observed in the outbreak of WS3 and WS4 at higher latitudes (Fig. 1e–i, k, l and Fig. 2). The resulting value of the mass flow is much lower than that used under the same numerical conditions to simulate the Great White Spots (GWSs)^{9,32} $Q = 2\text{--}3 \times 10^{11} \text{ m}^3 \text{ s}^{-1}$ (for GWS1960), $1\text{--}3 \times 10^{12} \text{ m}^3 \text{ s}^{-1}$ (GWS1990) and $2\text{--}5 \times 10^{11} \text{ m}^3 \text{ s}^{-1}$ (GWS2010). This means that WS1 and WS2 require about ~ 0.01 in mass flow compared to that necessary to produce the non-equatorial GWS cases (that is, those closer in latitude to the present one) that erupted in the years 1960 and 2010. In Supplementary Fig. 6, we present simulations of WS1 for an ample range of values for Q and for three close but different latitudes in the wind profile. The figure shows how sensitive the model results to both parameters (Q and φ or zonal velocity) are, thus constraining the Q value required to form the storm.

In the EPIC model, we simulated the outbreaks of WS1 and WS2 as single convective sources. We also tested the case of an outbreak inside a cyclonic vortex, as it was observed in the case of WS1 (Fig. 3). In order to get a realistic PV field that resembles the observed cloud morphology, we require energy inputs $E = 1\text{--}1.5 \text{ W kg}^{-1}$ for the WS1 and WS2 storms, injected in a small region of size $\sim 150 \text{ km}$. In the simulations, the disturbance expands horizontally in few days, as shown in the PV field. In the case of the outbreak triggered within a cyclone (which we take to be 1,500 km long and 500 km wide), the required value for the storm is similar both in energy and in extension, but under these circumstances, the storm PV field remains linked to the cyclone (although expanding around it) and the cyclone survives the eruption (Supplementary Fig. 7). The required energy is again much lower than that used under

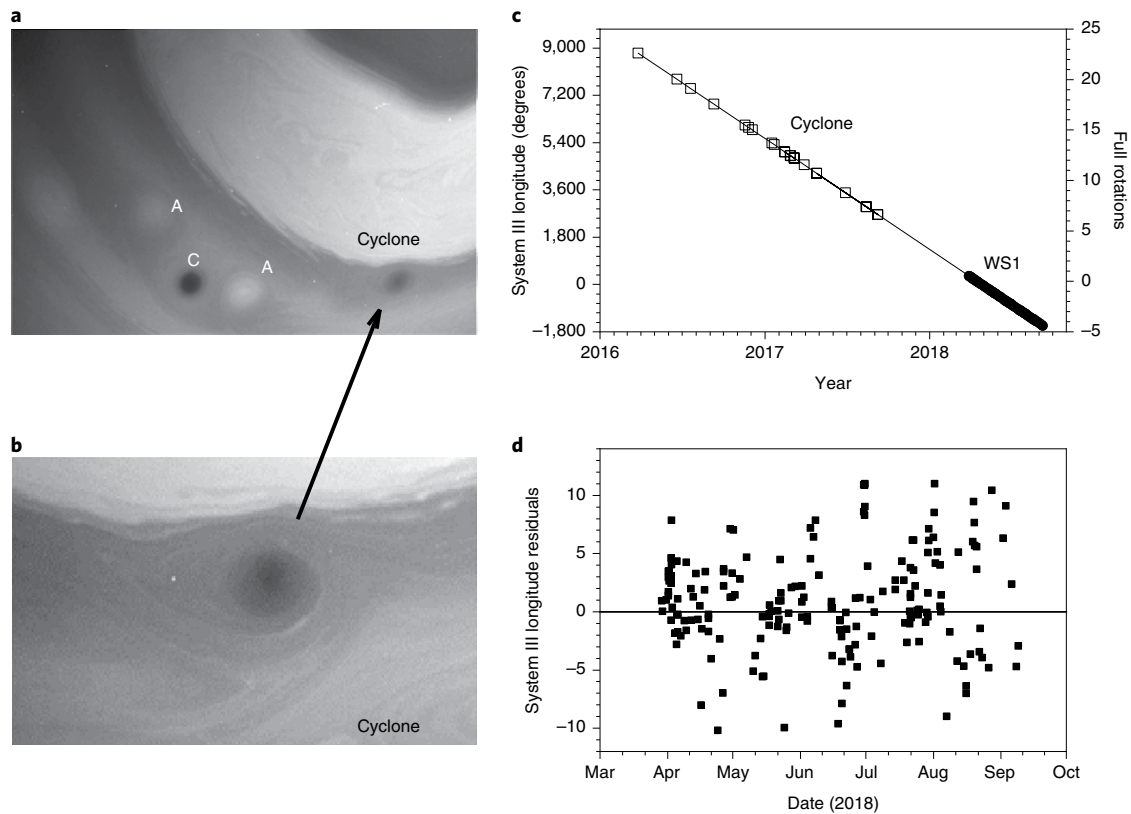


Fig. 3 | Convective onset in a compact cyclone. **a**, Cassini ISS image showing the ACA system²² and the cyclone where WS1 erupted. Image obtained on 7 March 2017, using the 889-nm methane band filter (MT3)⁷ (Cassini image number W1867560436_1.IMG). **b**, Detail showing the cyclone. Image obtained on 13 February 2007, using the same filter (Cassini image number W1865704116_1.IMG). **c**, Longitude drift of the cyclone (squares) and WS1 (dark spots) and linear fit to the data. A total of 39 images of the cyclone were used spanning the period from 25 March 2016 to 8 September 2017. **d**, Residuals in System III longitude between the extended linear fit of the cyclone drift and the measured longitude of the storm WS1. No error bars are shown for the y axis in **c** since they are similar to the size of the dot representing each measurement.

the same numerical conditions to simulate the 2010 GWS⁶ of $E = 500\text{--}1,000 \text{ W kg}^{-1}$ injected in a Gaussian region with a size $\sim 3,000 \text{ km}$. In Supplementary Fig. 8, we present simulations of WS1 triggered inside the cyclone for an ample range of values for E , showing again how sensitive model results are to the energy injection, therefore constraining the E value required to form the storm. We conclude from both models that the best simulations of the cloud morphologies of WS1 and WS2 require disturbances with lower integrated amplitudes $\sim 0.01\text{--}0.001$ in Q and E than storms of the GWS type. The simulations also require that the injection occurs continuously at the latitude and velocity observed for WS1 and WS2 (within the uncertainty in error bars; see Table 1 and Fig. 5 caption).

Saturn's seasons and convective-storm outbreaks

The 2018 storms emerged at the same season on Saturn as the 1960 GWS (orbital heliocentric longitude $L_s = 109^\circ$ for 1960 and 100° for 2018)⁹ (Fig. 6). The 1960 GWS occurred southwards of WS1 at latitude around $+58^\circ$ —that is, on the equatorial side of the double wind jet, moving with $u \approx 4 \text{ m s}^{-1}$ (Fig. 2)^{9,33}. The two main spots forming the 1960 GWS had a much larger zonal size of $\sim 35\text{--}45^\circ$ —that is, around four times the size of the 2018 WS1 and WS2 storms—and they grew faster than them, both in zonal and meridional extension³⁴. These properties, supported by the simulations described above, indicate that the 2018 event was of lower intensity than the 1960 GWS. The 2018 storms could have certain similarities with a middle-size convective storm that occurred in 1994 at 56° S ³⁵.

That storm exhibited zonal expansion, although the information we have for that case is very scarce. On the other hand, the 2018 event is different to the kind of disturbance that took place in 2015, which involved at least four vortices²² and did not appear to have a convective origin. We propose that the 2018 storms represent an intermediate case of a convective disturbance between a classical GWS planetary-scale phenomenon and the smaller-scale convective activity observed by Voyager 1 and 2 in 1980–1981^{1–3} and by Cassini in 2004–2009^{7,10,11,15} (Fig. 6).

It is remarkable that the 2018 event emerged 58 years (~ 2 Saturn years = 58.89 years) after the 1960 GWS, in agreement with the cycle observed in the equatorial GWSs^{9,33}, as proposed by a coupled radiative-thermodynamic moist convection model¹⁶. The outburst of WS1 and WS2 follows the global 30-year cycle of all the observed GWSs (except for the 2010 case that occurred in advance). We might speculate that the convective activity in 2018 was of lower intensity than that of 1960 due to the outbreak of the 2010 GWS at 38.2° N , which erupted about 7.3 years earlier and 30° to the south, and which could have altered the hypothetical cyclic properties of the GWSs. The lower intensity of WS1 and WS2 could be due to this previous outbreak, which could have limited the convective available potential energy^{16,24} and changed the thermodynamic conditions in the region needed to favour a major storm outbreak. In any case, the intensity, planetary distribution and cyclic behaviour of Saturn's convective storms represent a challenge in relation to the influence of the seasonal insolation and thermodynamic cycles in this complex multi-cloud-layer moist convective atmosphere.

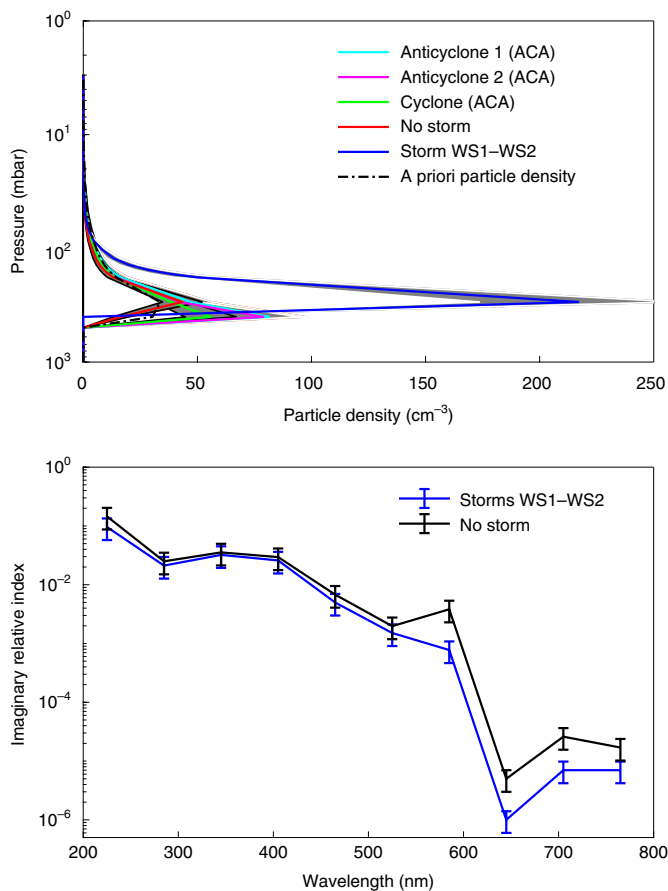


Fig. 4 | Vertical cloud structure and particle imaginary refractive index. Radiative transfer model results based on HST images. **a**, Particle density as a function of height (altitude increasing with decreasing pressure) in the storm and four different surrounding areas as indicated in the inset. The a priori particle density assumed for the model retrieval is also indicated. **b**, Imaginary refractive index versus wavelength for particles in the storm and in a surrounding area. See also Supplementary Fig. 5. The error band (particle density) and error bars (imaginary refractive index) are 1σ errors computed following refs. ^{25,26}.

In the near future, the almost continuous survey of the planet with ground-based telescopes¹⁷ (see Methods) will advance the knowledge of the rate of formation of different types of convective storms on Saturn, their dependence on the seasonal insolation cycle and their role in atmospheric dynamics. Moreover, different instruments on board the James Webb Space Telescope (JWST)³⁶ and giant telescopes on Earth observing in the infrared will allow retrieving other properties of the storms such as the presence of water or ammonia ice in their clouds, variations in their chemical composition and the thermal effects they can produce in the atmosphere. In any case, the observation of these phenomena in Saturn will be affected by the viewing geometry of the planet due to its rotation axis tilt relative to the orbital plane and ring shadowing, strongly limiting the area surveyed in the atmosphere (Supplementary Fig. 9).

Methods

Image data and measurement. Ground-based images used in this study were obtained by employing the ‘lucky imaging’ method³⁷. Most telescopes employed were in the 0.3–0.5-m diameter range (Supplementary Table 1). D. Peach contributed a set of images obtained using Chilescope (<http://www.chilescope.com/>), a remotely controlled 1-m telescope. The images span the spectral ranges ~450–650 nm (from colour composites red–green–blue, RGB) and the near infrared (~685–980 nm), including a few obtained at the 890-nm methane

absorption band. The list of contributors to ALPO-Japan and PVOL2 databases whose images were used in this study is given in Supplementary Table 1. More than ~1,500 individual longitude–latitude feature measurements were acquired along the 353 observing days. Images were navigated to fix the Saturn disk using WinJupos free software³⁸ and in most cases reprocessed to increase the contrast of weak features. PlanetCam images, obtained with the 2.2-m Calar Alto telescope, cover two spectral ranges (visible, 380–1,000 nm) and short wave infrared (SWIR, 1–1.7 μm) at specific selected wavelengths¹⁸. HST/WFPC images in this work span the wavelength range 225–763 nm in selected spectral bands³⁹ (Supplementary Fig. 5). The Cassini ISS images we employed to track back in time the position of the precursor cyclone to the first storm outbreak were obtained in the MT3 filter (central wavelength 889 nm) between April and September 2017³⁹ (Fig. 3). Strip maps of the region were constructed for identification and direct measurements of the images were performed using the Planetary Laboratory for Image Analysis (PLIA) software⁴⁰ and WinJupos (Supplementary Fig. 1).

Radiative transfer analysis. HST images have been calibrated in absolute reflectivity following standard procedures⁴¹. For every image, the reflectivity values of the storm have been measured, as well as their emission and incidence angles. Such values were fitted to Minnaert’s law^{24,26}, and nadir-viewing reflectivity (I/F)₀ and limb darkening parameter k were retrieved. We computed the expected values of reflectivity for the storm using those Minnaert parameters for three geometries ($\mu = 0.725$ and $\mu_0 = 0.786$; $\mu = 0.555$ and $\mu_0 = 0.632$; $\mu = 0.448$ and $\mu_0 = 0.511$ (where μ is the cosine of the emission angle and μ_0 the cosine of the incidence angle). These values sample the observed positions of the disturbance within the plane-parallel approximation. Finally, we took as a reference the undisturbed background atmosphere at 69° N, close to the latitude of the storms. In order to capture the centre to limb variation for the reference atmosphere, we selected 18 longitude points along this region covering in total 284° in System III longitudes. Our goal was to reproduce the observed reflectivity and limb-darkening for all filters simultaneously, both for the storm and for the reference atmosphere. We used the radiative transfer code and retrieval suite NEMESIS²⁵, which uses the optimal estimator scheme to find the most likely model to explain the observations. This version of the code assumes a plane-parallel atmosphere for scattering, uses a doubling/adding scheme, and considers the Rayleigh scattering due to the mixture of H₂ and He as well as the absorption due to CH₄, with a volume mixing ratio of 4.7×10^{-3} relative to H₂ (ref. ⁴²). The thermal profile, which has little impact on the absorption coefficients at these wavelengths, was taken from ref. ⁴³ and extrapolated adiabatically. The overall assumptions and fitting strategy were the same as in a previous works^{26,44}. Supplementary Tables 2,3 give the values used for the a priori assumptions and best-fitting results, respectively.

Dynamical analysis and numerical simulations. For the dynamical models, we used the wind profile measured with Cassini ISS²⁰ that is continuously forced. A parallel version of the SW model³² was run with a resolution of 0.1 deg pix⁻¹ and time step of 60 seconds, about one half of the maximum allowed by the Courant–Friedrichs–Lewy condition. Since the numerical integration is performed with fully explicit schemes, the parallelization with a domain-decomposition strategy is very efficient. The disturbance was kept active during the whole simulation time. The model uses periodic conditions in longitude and full-slip (reflective) in latitude. No topography is present. The EPIC model³¹ was run with a horizontal resolution of 0.12×0.06 deg pix⁻¹ and five vertical layers centred on a pressure level of 260 mbar. The vertical shear of the zonal wind was null across the layers and the Brunt–Väisälä frequency was set at $N = 0.007 \text{ s}^{-1}$ as in previous works on Saturn^{6,32}. In the SW model, the Rossby radius of deformation is $L_r = (gH)^{1/2}/f \approx 230 \text{ km}$, (gravity $g = 10 \text{ m s}^{-2}$, SW layer depth $H = 500 \text{ m}$, Coriolis parameter $f = 3.05 \times 10^{-4} \text{ s}^{-1}$), comparable to that obtained for the 2010 GWS (200 km $\leq L_r \leq 600 \text{ km}$). Note that this Rossby deformation radius is the one used in the SW model (and not that of the real atmosphere). The Rossby deformation radius in the EPIC model is $L_r = NH/f \approx 1,000 \text{ km}$ ($H \approx 40 \text{ km}$ is the scale height). Further details of the range of values of the parameters used in the simulations are given in Supplementary Tables 4.1 and 4.2.

Data availability

The data that support the plots within this paper and other findings of this study are available from the corresponding author on reasonable request. This work relies on images that can be downloaded from the following sources (see Supplementary Information for further details): ALPO-Japan (<http://alpo-j.asahikawa-med.ac.jp/Latest/Saturn.html>); PVOL2 database (<http://pvol2.ehu.es/pvol2/>); HST-OPAL programme (<https://archive.stsci.edu/prepds/opal/>); and Cassini ISS images at NASA Planetary Data System (<https://pds-imaging.jpl.nasa.gov/volumes/iss.html>). PlanetCam images are available from the corresponding author.

Code availability

The shallow water model code³⁰ is available from E.G.-M. (enrique.garcia.melendo@upc.edu) on request. The radiative transfer code NEMESIS (<http://users.ox.ac.uk/~atmp0035/nemesis.html>) is available on request from P.Irwin (patrick.irwin@physics.ox.ac.uk). The EPIC numerical model³¹ is an open-code funded by NASA; see details: <http://surveygizmoresponseuploads.s3.amazonaws.com>.

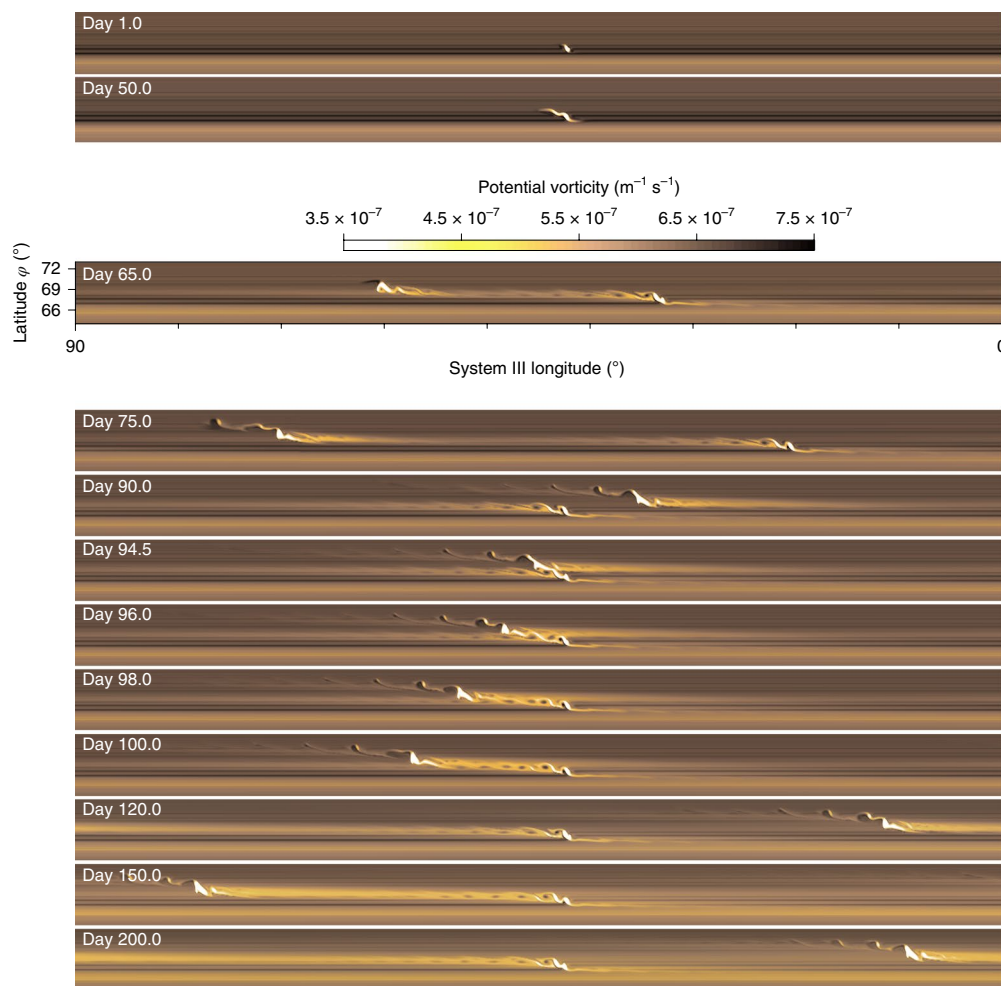


Fig. 5 | Numerical simulations of the disturbances generated by the storm outbreaks. Shallow water model for WS1 (latitude 67.7° N, zonal velocity $+59.8 \text{ m s}^{-1}$, mass rate injection $Q = 4 \times 10^9 \text{ m}^3 \text{ s}^{-1}$) and WS2 (latitude 68.9° N, zonal velocity $= +14.2 \text{ m s}^{-1}$, $Q = 2 \times 10^9 \text{ m}^3 \text{ s}^{-1}$) with a temporal duration of 200 days. On the frame corresponding to day 65, we include on the right the wind zonal profile portion covered by the simulation domain, with a velocity range in the 96 m s^{-1} to -12 m s^{-1} interval. In the model, both disturbances are injected continuously, moving with respect to rotation System III²¹ with the velocity that was measured on Saturn's atmosphere. For the sake of readability, WS1 is placed on the centre longitude in all frames except the 65- and 75-day frames, where the centre of the domain is approximately in the middle between the two storms. The interaction resulting from an encounter between both storms can be seen in days 94.5 to 100.

[com/fileuploads/15647/4054745/254-fd0a70105de25e281834d7f5dccc5451c_DowlingTimothyE.pdf](https://www.nature.com/fileuploads/15647/4054745/254-fd0a70105de25e281834d7f5dccc5451c_DowlingTimothyE.pdf)

Received: 28 December 2018; Accepted: 13 September 2019;
Published online: 21 October 2019

References

- Sromovsky, L. A. et al. Voyager 2 observations of Saturn's northern mid-latitude cloud features: morphology, motions, and evolution. *J. Geophys. Res.* **88**, 8650–8666 (1983).
- Ingersoll, A. P., Beebe, R. F., Conrath, B. J. & Hunt, G. E. in *Saturn* (eds Gehrels, T. & Matthews, M. S.) 195–238 (Univ. Arizona Press, 1984).
- Sánchez-Lavega, A., Rojas, J. F. & Sada, P. V. Saturn's zonal winds at cloud level. *Icarus* **147**, 405–420 (2000).
- Sánchez-Lavega, A. et al. A strong decrease in Saturn's equatorial jet at cloud level. *Nature* **423**, 623–625 (2003).
- Sánchez-Lavega, A. et al. Saturn's cloud morphology and zonal winds before the cassini encounter. *Icarus* **170**, 519–523 (2004).
- Sánchez-Lavega, A. et al. Deep winds beneath Saturn's upper clouds from a seasonal long-lived planetary-scale storm. *Nature* **475**, 71–74 (2011).
- Porco, C. C. et al. Cassini imaging science: Initial results on Saturn's atmosphere. *Science* **307**, 1243–1247 (2005).
- Sayanagi, K. M. et al. Dynamics of Saturn's great storm of 2010–2011 from Cassini ISS and RPWS. *Icarus* **223**, 460–478 (2013).
- Sánchez-Lavega, A. et al. in *Saturn in the 21st Century* (eds Baines, K. H. et al.) 377–416 (Cambridge Univ. Press, 2019).
- Dyudina, U. A. et al. Lightning storms on Saturn observed by Cassini ISS and RPWS during 2004–2006. *Icarus* **190**, 545–555 (2007).
- Dyudina, U. A. et al. Detection of visible lightning on Saturn. *Geophys. Res. Lett.* **37**, L09205 (2010).
- Fischer, G. et al. A giant thunderstorm on Saturn. *Nature* **475**, 75–77 (2011).
- Sánchez-Lavega, A. & Battaner, E. The nature of Saturn's great white spots. *Astron. Astrophys.* **185**, 315–326 (1987).
- Hueso, R. & Sánchez-Lavega, A. A three-dimensional model of moist convection for the giant planets II: Saturn's water and ammonia moist convective storms. *Icarus* **172**, 255–271 (2004).
- Del Genio, A. D. et al. in *Saturn after Cassini-Huygens* (eds Dougherty, M., Esposito, L. & Krimigis, T.) 113–159 (Springer, 2009).
- Li, C. & Ingersoll, A. P. Moist convection in hydrogen atmospheres and the frequency of Saturn's giant storms. *Nat. Geosci.* **8**, 398–403 (2015).
- Hueso, R. et al. The Planetary Virtual Observatory and Laboratory (PVOL) and its integration into the Virtual European Solar and Planetary Access (VESPA). *Planet. Space Sci.* **150**, 22–35 (2018).
- Mendikoa, I. et al. PlanetCam UPV/EHU: A two channel lucky imaging camera for Solar System studies in the spectral range 0.38–1.7 μm . *Pub. Astron. Soc. Pacific* **128**, 035002 (2016).
- Simon, A. A., Wong, M. H. & Orton, G. S. First Results from the Hubble OPAL program: Jupiter in 2015. *Astrophys. J.* **812**, 51S (2015).

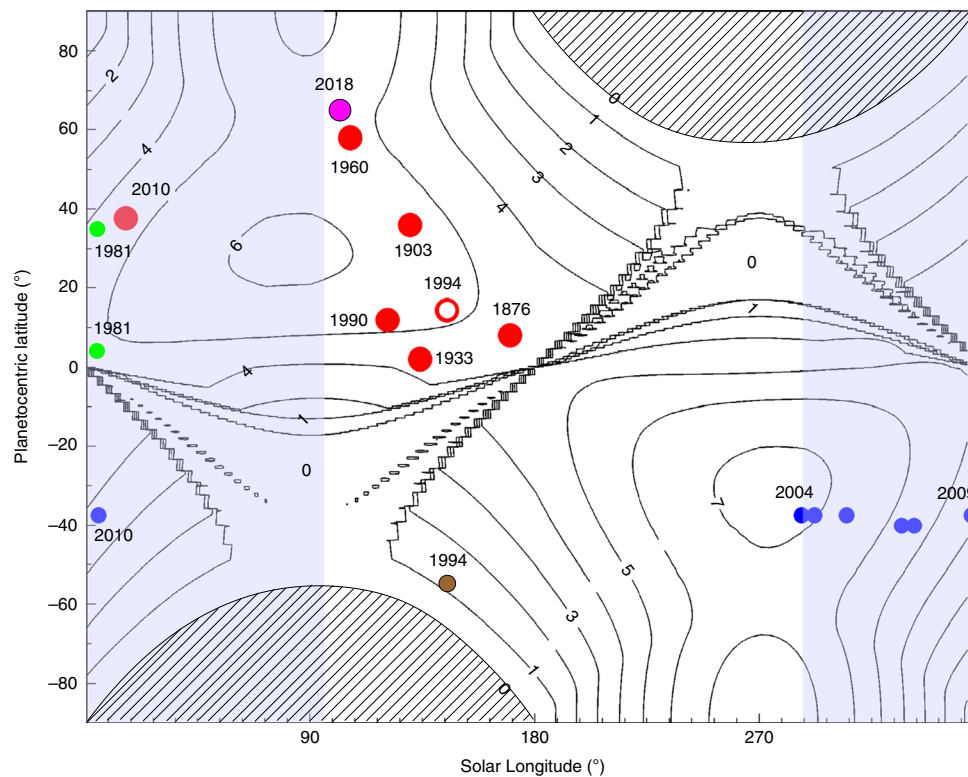


Fig. 6 | Seasonal insolation at the top of Saturn's atmosphere and convective events. Lines give the insolation in W m^{-2} along a Saturn year represented in terms of the orbital heliocentric longitude (L_5), where $L_5 = 0^\circ$ is the northern vernal equinox, 90° is the northern summer solstice, 180° is the northern autumnal equinox and 270° is the northern winter solstice. The major convective storms, the GWSs, are represented by red dots (year indicated), including a large equatorial storm in 1994 (red circle³⁵) probably related to the 1990 GWS event. The mid-scale storms were observed by Voyager 1 and 2 in 1980–1981 (green¹⁻³), with ground-based telescopes and HST in 1994 (brown³⁵) and with Cassini ISS in 2004–2010 (blue^{70,11}). The 2018 storms are represented by the magenta dot (year indicated). The shaded polar region mark the night-time periods. The blue area marks the period of full Cassini imaging coverage. In Supplementary Fig. 9 we illustrate the visibility of the Saturn disk due to changing geometry along the planet's orbit. Adapted from ref. ⁹, Cambridge Univ. Press.

20. García-Melendo, E. et al. Saturn's zonal wind profile in 2004–2009 from Cassini ISS images and its long-term variability. *Icarus* **215**, 62–74 (2011).
21. Archinal, B. A. et al. Report of the IAU working group on cartographic coordinates and rotation elements: 2015. *Celest. Mech. Dyn. Astr.* **130**, 22 (2018).
22. del Río-Gaztelurrutia, T. et al. A planetary-scale disturbance in a long living three vortex coupled system in Saturn's atmosphere. *Icarus* **302**, 499–513 (2018).
23. Fletcher, L. N. et al. Moist convection and the 2010–2011 revival of Jupiter's South Equatorial Belt. *Icarus* **286**, 94–117 (2017).
24. Sánchez-Lavega, A. *An Introduction to Planetary Atmospheres* 118–121, 376–377 (CRC, 2011).
25. Irwin, P. G. J. et al. The NEMESIS planetary atmosphere radiative transfer and retrieval tool. *J. Quant. Spectrosc. Radiat. Transf.* **109**, 1136–1150 (2008).
26. Sanz-Requena, J. F. et al. Haze and cloud structure of Saturn's North Pole and Hexagon Wave from Cassini/ISS imaging. *Icarus* **305**, 284–300 (2018).
27. Sánchez-Lavega, A., Pérez-Hoyos, S. & Hueso, R. Condensate clouds in planetary atmospheres: a useful application of the Clausius–Clapeyron equation. *Am. J. Phys.* **72**, 767–774 (2004).
28. West, R. A., Baines, K. H., Karkoschka, E. & Sánchez-Lavega, A. in *Saturn after Cassini-Huygens* (eds Dougherty, M., Esposito, L. & Krimigis, T.) 161–179 (Springer, 2009).
29. Sromovsky, L. A., Baines, K. H. & Fry, P. M. Models of bright storm clouds and related dark ovals in Saturn's Storm Alley as constrained by 2008 Cassini/VIMS spectra. *Icarus* **302**, 360–385 (2018).
30. García-Melendo, E. & Sánchez-Lavega, A. Shallow water simulations of Saturn's giant storms at different latitudes. *Icarus* **286**, 241–260 (2017).
31. Dowling, T. E. The Explicit Planetary Isentropic-Coordinate (EPIC) atmospheric model. *Icarus* **132**, 221–238 (1998).
32. García-Melendo, E. et al. Atmospheric dynamics of Saturn's 2010 giant storm. *Nat. Geosci.* **6**, 525–529 (2013).
33. Sánchez-Lavega, A. Saturn's great white spots. *Chaos* **4**, 341–353 (1994).
34. Dollfus, A. Mouvements dans l'atmosphère de Saturne en 1960. Observations coordonnées par l'Union Astronomique Internationale. *Icarus* **2**, 109–114 (1963).
35. Sánchez Lavega, A. et al. Large-scale storms in Saturn's atmosphere during 1994. *Science* **271**, 631–634 (1996).
36. Norwood, P. et al. Giant planet observations with the James Webb Space Telescope. *Pub. Astron. Soc. Pac.* **128**, 018005 (2016).
37. Mousis, O. et al. Instrumental methods for professional and amateur collaborations in planetary astronomy. *Exp. Astron.* **38**, 91–191 (2014).
38. Hahn, G. & Jacquesson, M. WinJUPOS. *Homepage Grischa Hahn* <http://www.grischa-hahn.homepage.t-online.de/> (2019).
39. Porco, C. C. et al. Cassini imaging science: instrument characteristics and anticipated scientific investigations at Saturn. *Space Sci. Rev.* **115**, 363–497 (2004).
40. Hueso, R. et al. The Planetary Laboratory for Image Analysis (PLIA). *Adv. Space Res.* **46**, 1120–1138 (2010).
41. Dressel, L. *Wide Field Camera 3 Instrument Handbook, Version 10.0* (Space Telescope Science Institute, 2018).
42. Fletcher, L. N. et al. Methane and its isotopologues on Saturn from Cassini/CIRS observations. *Icarus* **199**, 351–367 (2009).
43. Lindal, G. F. et al. The atmosphere of Saturn – an analysis of the Voyager radio occultation measurements. *Astron. J.* **90**, 1136–1146 (1985).
44. Pérez-Hoyos, S. et al. Saturn's tropospheric particles phase function and spatial distribution from Cassini ISS 2010–11 observations. *Icarus* **277**, 1–18 (2016).

Acknowledgements

This work has been supported by the Spanish project AYA2015-65041-P (MINECO/FEDER, UE) and Grupos Gobierno Vasco IT-366-19. A list of the sources for the images used in this paper can be found in the Supplementary Information. This work used data acquired from the NASA/ESA HST Space Telescope, associated with OPAL programme (principal investigator: Simon, GO13937), and archived by the Space Telescope Science Institute, which is operated by the Association of Universities for Research in Astronomy, Inc., under NASA contract no. NAS 5-26555. All OPAL maps are available at <https://doi.org/10.17909/T9G593>, and M.H.W. and A.A.S. acknowledge financial support from his programme. M.H.W. through a grant from the Space Telescope Science Institute, which is operated by AURA under NASA contract NAS 5-26555.

Author contributions

A.S.-L. directed the work, made the features tracking measurements, retrieved the winds and interpreted the results. E.G.-M., M.S. and J.L. performed the shallow water and EPIC numerical simulations. T.d.R.-G. performed the Cassini image analysis of the storm precursor. R.H., J.M.G.-F., T.B., M.D. contributed to the analysis of ground-based observations. J.F.S.-R. and S.P.-H. performed the radiative transfer analysis. A.A.S. and M.H.W. performed the HST observations and helped in their analysis. K.M.S., J.J.B. and J.L.G. mapped and analyzed Cassini ISS images. U.D. and S.E. designed the ISS observation sequences. All authors discussed the results and contributed to preparing the manuscript.

Competing interests

The authors declare no competing interests.

Additional information

Supplementary information is available for this paper at <https://doi.org/10.1038/s41550-019-0914-9>.

Correspondence and requests for materials should be addressed to A.S.-L. or E.G.-M.

Peer review information *Nature Astronomy* thanks Cheng Li and the other, anonymous, reviewer(s) for their contribution to the peer review of this work.

Reprints and permissions information is available at www.nature.com/reprints.

Publisher's note Springer Nature remains neutral with regard to jurisdictional claims in published maps and institutional affiliations.

© The Author(s), under exclusive licence to Springer Nature Limited 2019